Optics and Lasers in Engineering 172 (2024) 107837

Contents lists available at ScienceDirect

Optics and Lasers in Engineering

journal homepage: www.elsevier.com/locate/optlaseng

Sculpting axial characteristics of incoherent imagers by hybridization methods

Shivasubramanian Gopinath [a], Aravind Simon John Francis Rajeswary [a], Vijayakumar Anand [a,b,*]

[a] Institute of Physics, University of Tartu, W. Ostwaldi 1, Tartu 50411, Estonia
[b] Optical Sciences Center and ARC Training Centre in Surface Engineering for Advanced Materials (SEAM), School of Science, Computing and Engineering Technologies, Swinburne University of Technology, Hawthorn, Melbourne, VIC 3122, Australia

ARTICLE INFO

Keywords:
Incoherent imaging
Digital holography
Computational imaging
Diffractive optics
Lucy-Richardson-Rosen algorithm
Non-linear reconstruction
Fresnel incoherent correlation holography
Coded aperture imaging

ABSTRACT

Axial resolving power (ARP) is one of the cornerstones of imaging systems. In conventional imaging systems, changing ARP by changing the numerical aperture affects also lateral resolving power (LRP). It is highly desirable to change ARP independent of LRP. Recently, incoherent digital holography (IDH) techniques were developed using sparse ensembles of Bessel, Airy and self-rotating beams that allow tuning ARP independent of LRP. In the above studies, the ARP was tuned by controlling the randomness which resulted in noisy reconstructions. In this study, we proposed and demonstrated two INCoherent Hybrid Imaging Systems (INCHIS) using a Bessel and spherical beam to change the ARP between the limits of Bessel and spherical beam independent of LRP. The first hybridization technique INCHIS-H1 requires pre-engineering of multifunctional phase masks using a recently developed modified Gerchberg-Saxton algorithm and an active device such as a spatial light modulator. The second hybridization technique INCHIS-H2 can be implemented using both active as well as passive optical elements with lens and axicon functions and the ARP is changed digitally after optical recording. While INCHIS-H1 requires pre-engineering of phase masks to change ARP like any conventional imaging system, the capability in INCHIS-H2 to change ARP post-recording opens a new pathway in imaging technology. Simulation results and proof-of-concept experimental results are presented. A recently developed Lucy-Richardson-Rosen algorithm has been used for image reconstruction for the above cases. We believe that the developed hybridization methods will revolutionize the field of IDH, computational imaging, computer vision and microscopy.

1. Introduction

A spatially incoherent and temporally coherent light source is preferred for imaging applications due to a higher resolution and lower imaging noises: speckle noise and edge ringing effects, in comparison to spatially and temporally coherent light sources. In this research, only imaging systems that use a spatially incoherent and temporally coherent source are considered. The lateral resolving power (LRP) and axial resolving power (ARP) are two of the most important characteristics of an imaging system given as $\sim\lambda/\mathrm{NA}$ and $\sim\lambda/\mathrm{NA}^2$ respectively, where NA is the numerical aperture given as $\sim D/2f$, where D is the diameter of the lens and f is the focal length. In all imaging systems, LRP and ARP are interdependent and changing one by changing NA affects the other [1]. In many scenarios, it is desirable to change one property without changing the other. For instance, in microscopy, when studying thick and sparse objects, it is desirable to decrease ARP without affecting the LRP so that the entire measurement can be completed within one or a few recordings. In direct imaging approach, an axicon with a long focal depth is often used to image objects with a low axial resolution (AR). However, the Bessel beam generated by an axicon has sidelobes which suppress the high spatial frequencies during imaging [2–5]. Either engineering approaches are needed to suppress the sidelobes [6] or deconvolution methods are needed to process the blurred images generated by Bessel beams [7]. Alternatives to Bessel beams to image objects with a high focal depth are available for direct imaging which includes axilens [8,9] and holographic beam shaping elements [10,11]. However, even in the above cases, post-processing techniques are necessary to obtain a high-quality image. In indirect imaging methods

* Corresponding author.
E-mail address: vijayakumar.anand@ut.ee (V. Anand).

https://doi.org/10.1016/j.optlaseng.2023.107837
Received 5 July 2023; Received in revised form 16 August 2023; Accepted 10 September 2023
Available online 20 September 2023

such as holography, the different planes of an object are observed digitally using computational refocusing in the form of numerical back propagation instead of manual refocusing as it is done in direct imaging methods [12–14]. Like direct imaging methods, holography methods also have the same relationship between LRP and ARP which makes tuning one property independent of another difficult.

Hybridization is a powerful technique used for creating mixed characteristics that are not naturally available and it means different things in different fields. In holography, hybridization approach uses combination of different types of optical fields in a special basis to create mixed imaging characteristics. Fresnel incoherent correlation holography (FINCH) is a widely used incoherent digital holography (IDH) technique [15,16]. In FINCH, light from an object point is split into two, differently modulated by two quadratic phase masks and interfered to create a self-interference hologram. The image of the object is then reconstructed by numerical back propagation of the hologram. FINCH, in inline configuration, requires at least three camera shots with different phase shifts followed by a computational superposition to reconstruct object information without twin image and bias terms. FINCH has a higher LRP but a lower ARP than those of direct incoherent imaging systems with the same NA. In FINCH, a hybridization method was applied by changing one of the two beam modulations from quadratic phase to a spiral phase to achieve edge enhancement in reconstructed images [17]. Another IDH technique called coded aperture correlation holography (COACH), was developed in 2016 which has the same LRP and ARP as those of direct incoherent imaging systems with the same NA [18]. A hybridization method was developed by combining FINCH and COACH such that the LRP and ARP can be tuned between the limits of FINCH and COACH [19]. This allows to create on-demand 3D imaging characteristics tailored for different studies. In the case of FINCH—COACH system, the change in ARP resulted in a change in LRP but the ARP-LRP pairs of the hybrid FINCH—COACH systems cannot be obtained naturally from either FINCH or COACH.

The development of COACH connected two sub-fields of imaging namely IDH and coded aperture imaging (CAI) as the hologram recording in COACH is similar to that in IDH but the reconstruction is similar to that in CAI [20–24]. Subsequently, interferenceless COACH (I-COACH) was developed which has the advantages of both IDH and CAI [25]. In I-COACH, the complete 3D information of an object was recorded without two-beam interference for the first time. The first version of I-COACH used a quasi-random phase mask and matched filter for image reconstruction and required at least three camera shots as FINCH and COACH [26]. Later, a new reconstruction method called non-linear reconstruction (NLR) was developed that enabled single shot capability in I-COACH [27]. With NLR, I-COACH was implemented with different deterministic optical fields such as Bessel, Laguerre-Gaussian and higher order Bessel beams, but the reconstruction was noisy [28]. Recently, a novel computational reconstruction method called Lucy-Richardson-Rosen algorithm (LR^{2}A) was developed by combining NLR and the widely used Lucy-Richardson algorithm (LRA) and implemented for 3D imaging using mid infrared optical fields with Cassegrain objective lenses as coded apertures [29–31]. The LR^{2}A method was found to perform better than NLR and LRA for deterministic optical fields [32–34]. As it is known, deterministic optical fields have many interesting propagation characteristics which can be exploited for imaging applications.

The capability to tune ARP independent of LRP has been demonstrated in I-COACH using a sparse array of Bessel beams [35], Airy beams [36] and self-rotating beams [37]. In this study, we propose and demonstrate two INCoherent Hybrid Imaging Systems (INCHIS) for tuning ARP independent of LRP using deterministic optical fields and LR^{2}A. In the first hybridization method INCHIS-H1, an IDH-like architecture has been used to convert every object point into at least two beams - Bessel and spherical and create a self-interference between them. The strength of the beams is controlled to tune the ARP between the limits of the Bessel beam and spherical beam. ARP can be tuned between the limits of CAI with Bessel and CAI with spherical beam and at all other points the system is IDH with self-interfering Bessel and spherical beams. In the second hybridization method INCHIS-H2, two camera shots of the same scene are recorded, one with an axicon and another with a lens and the ARP is engineered after recording by controlling the strength of the two intensity distributions. Once again, the tunability range is within the AR limits of axicon and a lens. INCHIS-H1 requires pre-engineering of masks, while INCHIS-H2 requires only post-engineering of holograms. *To the best of our knowledge, this is the first time, a method has been demonstrated to engineer the AR of recorded pictures and videos allowing to focus and defocus different planes relative to one another*. This is different from the deconvolution methods developed to digitally refocus information, as in such methods, when one plane is focused, other planes are blurred [32]. But in the developed method, it is possible to change ARP which allows to simultaneously digitally refocus multiple planes and refocus one plane with respect to another. There are other methods developed by Rai and Rosen [38] and our group [37] which are originally developed for real time tuning of ARP and for separating objects with same lateral locations, can be efficiently adapted for tuning ARP after completing the recording process. However, the post tuning is complicated unlike INCHIS-H2 and both methods cannot be implemented using refractive elements.

The manuscript consists of six sections. The methodology for the two hybridization methods is presented in the second section. The simulation studies and results are presented in the third section. In the fourth section, proof-of-concept experimental results are presented. The results are discussed in the fifth section. The conclusion and future perspectives of the study are presented in the final section.

2. Methodology

The optical configuration of INCHIS-H1 and INCHIS-H2 are shown in Figs. 1 and 2 respectively. In INCHIS-H1, the pure optical fields for hybridization are selected in the first step and the corresponding phase masks are calculated [39]. The phase-only masks for generating pure optical fields are multiplexed into a pure phase mask using the recently developed computational algorithm, transport of amplitude into phase based on Gerchberg-Saxton algorithm (TAP-GSA) [40,41]. This is a necessary step as combining two pure phase functions result in a complex function which is difficult to implement in experiments. If random multiplexing was used to combine two pure phase functions, it leads to scattering noises and decreases light throughput [41]. It is possible to multiplex several phase masks using TAP-GSA. However, in this study, only two optical fields are considered for both methods. The strengths of the two masks are controlled by two variables namely T_1 and T_2. The resulting phase-only masks from TAP-GSA is displayed on a spatial light modulator (SLM) and the point spread function (I_{PSF}) library is recorded at different depths using a point object. Then an object is recorded with the same mask and exactly same experimental conditions. The 3D image of the object can be reconstructed by processing the I_{PSF} library and object intensity distribution using one of the reconstruction methods such as matched filter, phase-only filter, NLR and LR^{2}A [26,28,29]. Depending upon T_1 and T_2, the ARP of the imaging system varies. When the phase mask is pure, i.e., either axicon or lens, then the system behaves similar to I-COACH and CAI as only a single beam is generated. When a hybrid mask is used, multiple beams are generated and self-interfered and the imaging system behaves similar to FINCH or COACH.

In INCHIS-H2, the light from an object point is split into two using a 50–50 beam splitter. The two identical object intensity distributions from the beam splitter is modulated by two active or passive optical elements: a lens and an axicon and the two point spread functions $I_{PSF\text{-}L}$ and $I_{PSF\text{-}A}$ are recorded under identical conditions. An object is recorded in the similar fashion. The point spread function and object intensity distributions are calculated by summing the contributions from lens and axicon after selecting the strengths T_1 and T_2 respectively. The image of

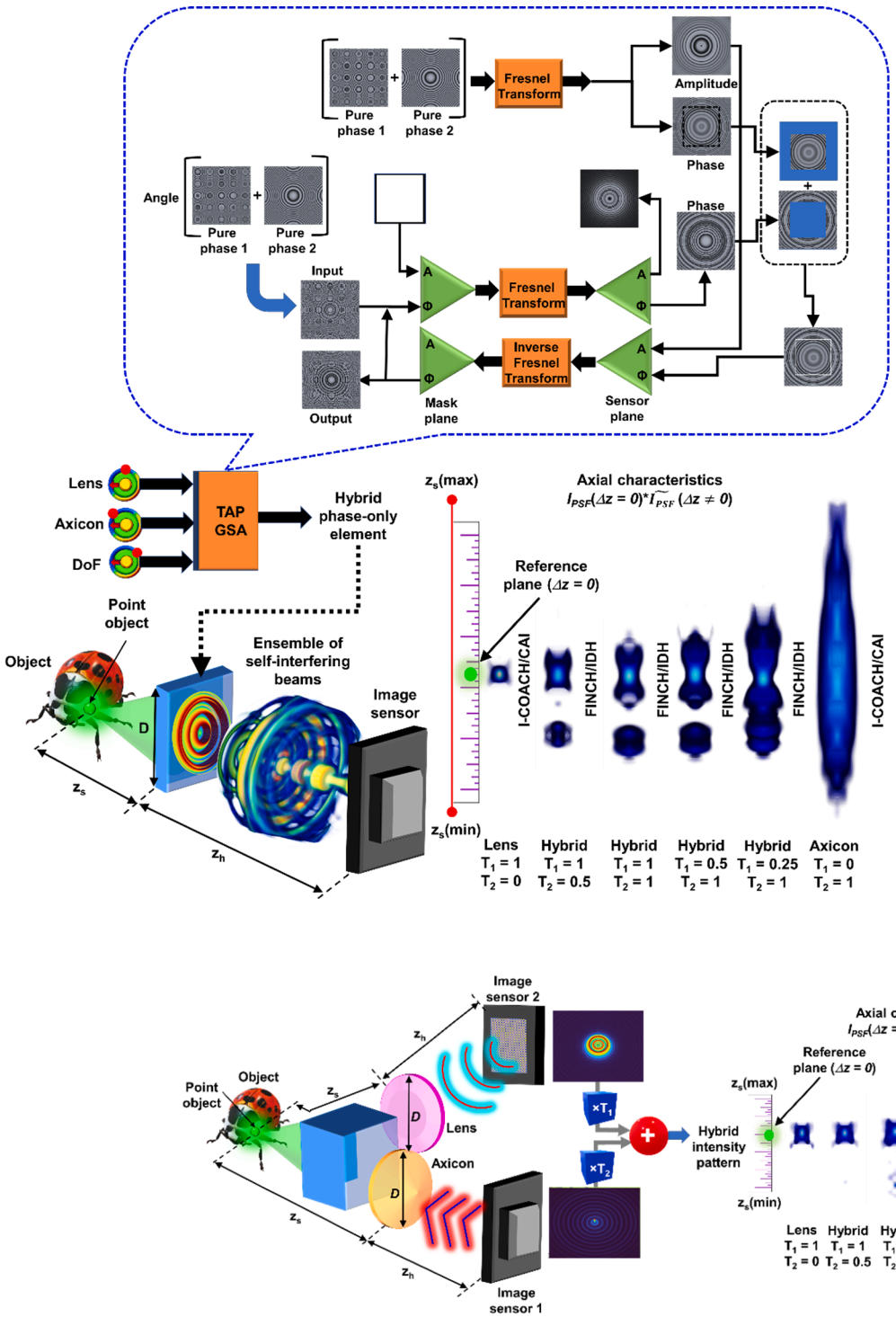

Fig. 1. Optical configuration of INCHIS-H1. z_s, z_h are object and image distances, D is the diameter of the aperture, TAP-GSA is transport of amplitude into phase based on Gerchberg-Saxton algorithm, I_{PSF} is the point spread intensity distribution, $\widetilde{I_{PSF}}$ is phase-only filtered version of I_{PSF}, $\Delta z = 0$ is the plane of interest, DoF is degrees of freedom and T_1 and T_2 are strengths of the phase modulators namely lens and an axicon respectively. The axial distributions were generated using a phase-only filter.

Fig. 2. Optical configuration of INCHIS-H2. z_s, z_h are object and image distances, D is the diameter of the aperture, I_{PSF} is the point spread intensity distribution, $\widetilde{I_{PSF}}$ is phase-only filtered version of I_{PSF}, $\Delta z = 0$ is the plane of interest, T_1 and T_2 are strengths of the intensity distributions of lens and an axicon respectively. The axial distributions were generated using a phase-only filter.

the object is then reconstructed by processing the I_{PSF} and object intensity distribution (I_O) using LR^{2}A [29]. After recording a scene in this fashion collinearly using an axicon and a lens simultaneously using two cameras under identical conditions, it is possible to engineer the ARP after recording.

2.1. INCHIS-H1

A point object located at $(\bar{r}_s, z_s)$ and emitting light with an amplitude of $\sqrt{I_s}$ is considered. A hybrid phase mask designed by combining the phase mask of a diffractive axicon and a diffractive lens using TAP-GSA is located at a distance of z_s from the point object. The complex amplitude of the hybrid phase mask is given as $\psi_M \approx \exp[-i\pi T_1(\lambda f)^{-1}(x^2 + y^2)] + \exp[-i2\pi T_2 \Lambda^{-1}\sqrt{x^2+y^2}]$, where f is the focal length of the

diffractive lens, Λ is the period of the diffractive axicon, λ is the wavelength, $0 \le T_1 \le 1$ and $0 \le T_2 \le 1$ and ψ_M is a phase-only function in experiment. For simplicity, only a single wavelength λ is considered. The variables T_1 and T_2 control the contributions from a diffractive lens and a diffractive axicon respectively. When $T_1 = 0$ and $T_2 = 1$, the hybrid phase mask reduces to a diffractive axicon and when and $T_1 = 1$ and $T_2 = 0$, the hybrid phase mask reduces to a diffractive lens and for other values of T_1 and T_2, a hybrid mask is obtained.

Since, TAP-GSA has been thoroughly investigated in [41], only the gist of the idea is presented here. A Fresnel propagator is used to connect the two planes of interest namely mask plane and sensor plane. The TAP-GSA begins with the mask plane with the phase of the ψ_M and propagated to the sensor plane by the Fresnel propagator. At the sensor plane, the amplitude information is replaced completely by the constraint which is the amplitude information obtained if ψ_M is propagated to the sensor plane by the Fresnel propagator. The obtained phase information is partially replaced by the phase information obtained at the sensor plane if ψ_M is propagated from the mask plane to the sensor plane by Fresnel propagator. The degrees of freedom (DoF) is the ratio between the number of pixels replaced in the phase matrix of the sensor by total number of pixels of the matrix. The resulting complex amplitude is back propagated to the mask plane by an inverse Fresnel propagator. The amplitude is replaced by a uniform matrix and the phase is carried on. After several iterations, the TAP-GSA converges and yields a phase-only function that can generate the optical fields corresponding to the complex amplitude formed by the direct summation of the two-parent pure-phase functions.

The complex amplitude after the hybrid phase mask is given as $\sqrt{I_s}C_1 L\left(\frac{\bar{r}_s}{z_s}\right) Q\left(\frac{1}{z_s}\right)\psi_M$, where L and Q are the linear and quadratic phase functions given as $L\left(\frac{\bar{s}}{z}\right) = \exp[i2\pi(\lambda z)^{-1}(s_x x + s_y y)]$ and $Q(b) = \exp[i\pi b\lambda^{-1}(x^2 + y^2)]$, respectively, and C_1 is a complex constant. A self-interference is obtained between the Bessel beam and spherical beam as both are derived from the same object point. The I_{PSF} recorded by the image sensor located at a distance of z_h is given as

$$I_{PSF}(\bar{r}_0;\bar{r}_s,z_s) = \left|\sqrt{I_s}C_1 L\left(\frac{\bar{r}_s}{z_s}\right) Q\left(\frac{1}{z_s}\right)\psi_M \otimes Q\left(\frac{1}{z_h}\right)\right|^2, \tag{1}$$

where, '$\otimes$' is a 2D convolutional operator and $\bar{r}_0 = (u, v)$ is the location vector in the sensor plane. Now substituting for ψ_M in Eq. (1), we obtain

$$I_{PSF}(\bar{r}_0;\bar{r}_s,z_s) = \left|\sqrt{I_s}C_1 L\left(\frac{\bar{r}_s}{z_s}\right) Q\left(\frac{1}{z_s}\right)\left\{\exp\left[-i\pi T_1(\lambda f)^{-1}\left(x^2+y^2\right)\right] + \exp\left[-i2\pi T_2\Lambda^{-1}\sqrt{x^2+y^2}\right]\right\} \otimes Q\left(\frac{1}{z_h}\right)\right|^2. \tag{2}$$

After grouping the individual contributions, we get

$$I_{PSF}(\bar{r}_0;\bar{r}_s,z_s) = \left|\sqrt{I_s}C_1 L\left(\frac{\bar{r}_s}{z_s}\right) Q\left(\frac{1}{z_s}\right)\exp\left[-i\pi T_1(\lambda f)^{-1}\left(x^2+y^2\right)\right] \otimes Q\left(\frac{1}{z_h}\right) + \sqrt{I_s}C_1 L\left(\frac{\bar{r}_s}{z_s}\right) Q\left(\frac{1}{z_s}\right)\exp\left[-i2\pi T_2\Lambda^{-1}\sqrt{x^2+y^2}\right] \otimes Q\left(\frac{1}{z_h}\right)\right|^2, \tag{3}$$

$$I_{PSF}(\bar{r}_0;\bar{r}_s,z_s) = \left|A_{DL} + A_{DA}\right|^2, \tag{4}$$

where A_{DL} and A_{DA} are the complex amplitudes with diffraction efficiencies corresponding to maximum phases ($2\pi T_1$) and ($2\pi T_2$) generated for the diffractive lens and diffractive axicon respectively and are a spherical beam given as $Q\left(\frac{1}{z_e}\right)$, where $\frac{1}{z_e} = \frac{1}{z_s} + \frac{1}{z_h} - \frac{1}{f}$ and a Bessel beam of first kind J_0. The transverse magnification of the system is given as $M_T = z_h/z_s$. The I_{PSF} can be expressed as

$$I_{PSF}(\bar{r}_0;\bar{r}_s,z_s) = I_{PSF}\left(\bar{r}_0 - \frac{z_h}{z_s}\bar{r}_s;0,z_s\right). \tag{5}$$

A 2D object consisting of M points can be represented as a collection of M Kronecker Delta functions as

$$o(\bar{r}_s) = \sum_j^M a_j\delta\left(\bar{r} - \bar{r}_{s,j}\right), \tag{6}$$

where $a_j^{'}s$ are constants. Since, in this study, only spatially incoherent illumination is considered, the light diffracted from one point do not interfere with light diffracted from another but their intensities add up in the sensor plane. Therefore, the object intensity distribution obtained for o can be expressed as

$$I_O(\bar{r}_0;z_s) = \sum_j^M a_j I_{PSF}\left(\bar{r}_0 - \frac{z_h}{z_s}\bar{r}_{s,j};0,z_s\right). \tag{7}$$

The goal is to reconstruct the object o from I_{PSF} and I_O given by Eq. (5) and Eq. (7) respectively. If the autocorrelation of I_{PSF} gives a Delta-like function, then the object o can be reconstructed by a cross-correlation between I_{PSF} and I_O. In a recent study, the use of NLR generated a sharp autocorrelation function and therefore reconstructed intensity distributions of multipoint objects effectively [28]. The reconstructed image by matched filter is given as

$$\begin{aligned} P(\bar{r}_R) &= \int\int I_O(\bar{r}_0;z_s) I^*_{PSF}(\bar{r}_0 - \bar{r}_R;z_s)d\bar{r}_0 \\ &= \int\int \sum_j a_j I_{PSF}\left(\bar{r}_0 - \frac{z_h}{z_s}\bar{r}_{s,j};z_s\right) I^*_{PSF}(\bar{r}_0 - \bar{r}_R;z_s)d\bar{r}_0, \\ &= \sum_j a_j\gamma\left(\bar{r}_R - \frac{z_h}{z_s}\bar{r}_{s,j}\right) \approx o\left(\frac{\bar{r}_s}{M_T}\right), \end{aligned} \tag{8}$$

where '$*$' means complex conjugate. For a speckle pattern, γ is a Delta-like function. But for most deterministic fields such as Gaussian, Bessel, Laguerre-Gaussian beams, etc., γ is not a Delta-like function. The reconstruction by NLR generates a Delta-like function for both random as well as deterministic optical fields. The reconstruction by NLR is given as

$$I_R = \left|\mathscr{F}^{-1}\left\{|\widetilde{I}_{PSF}|^{\alpha}\exp[j\cdot\arg(\widetilde{I}_{PSF})]|\widetilde{I}_O|^{\beta}\exp[-j\cdot\arg(\widetilde{I}_O)]\right\}\right|, \tag{9}$$

where α and β are tuned between -1 and 1 until the lowest reconstruction noise quantified by the entropy is obtained, $\widetilde{I}$ is the Fourier transform of I and arg(•) is the phase. In recent studies, an algorithm LR^{2}A developed by combining the LRA with NLR yielded a better signal to noise ratio (SNR) than NLR [29,32-34]. The schematic of LR^{2}A is shown in Fig. 3. The algorithm uses a maximum likelihood solution estimation by iteration of the existing relationship between the object o, I_{PSF} and I_O. The algorithm begins with an initial guessed solution of o which is usually I_O ($R^{p=1}$) and is convolved with I_{PSF} and the resulting matrix is compared with I_O by calculating the ratio. This ratio is correlated with the I_{PSF} to obtain the residue and multiplied to the previous solution which is $R^{p=1}$. The process is repeated until the solution converges to a non-changing value. The LRA uses matched filter for performing the correlation which is replaced by NLR to obtain LR^{2}A.

Within the focal depth of the Bessel beam, the A_{DA} remains a constant, while A_{DL} varies. By controlling T_1 and T_2, I_{PSF} can be shifted towards the behaviors of A_{DA} and A_{DL}. When the system is shifted towards A_{DL}, I_{PSF} changes with z_s and so it is necessary to record I_{PSF} for all values of z_s. On the other hand, when the system is shifted towards A_{DA}, I_{PSF} does not change with z_s and so I_{PSF} recorded for one z_s can be used to reconstruct all if not most of the object planes. Unlike the case with A_{DL}, with A_{DA}, the object information is not blurred or unrecognizable but has a low resolution due to suppression of higher spatial frequencies [7, 28].

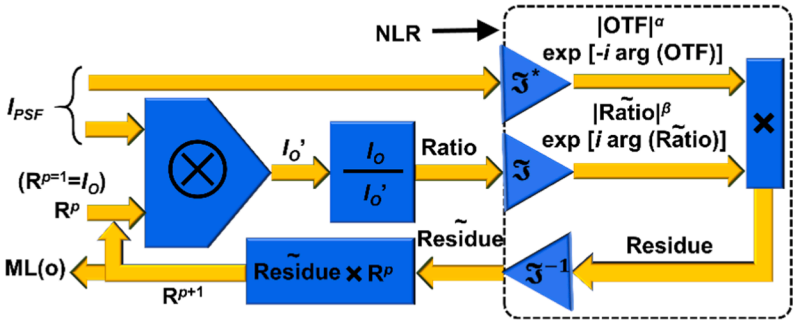

Fig. 3. Schematic of LR^{2}A. ML—maximum likelihood; OTF—optical transfer function; p—number of iterations; $\otimes$—2D convolutional operator; $\Im$ - Fourier transform, $\Im^*$ - complex conjugate operation following a Fourier transform, $\Im^{-1}$ – inverse Fourier transform, R^p and $R^{(p+1)}$ are the p^{th} and $(p+1)^{\text{th}}$ solutions, I_O was used as the initial guess solution $R^{p=1}$, $\sim$ Fourier transform of a variable.

2.2. INCHIS-H2

A point object located at $(\bar{r}_s, z_s)$ is considered. It emits light with an amplitude of $\sqrt{I_s}$. The light from the point object is split into two using a 50–50 beam splitter. One of the two parts was modulated by a lens and another by an axicon both located at a distance of z_s from the point object. Two identical image sensors are mounted at a distance of z_h from the lens and the axicon respectively such that their optical axes are overlapped. The complex amplitude after the lens and the axicon are given as $\sqrt{I_s/2}C_1 L\left(\frac{\bar{r}_s}{z_s}\right) Q\left(\frac{1}{z_s}\right) \exp[-i\pi(\lambda f)^{-1}(x^2+y^2)]$ and $\sqrt{I_s/2}C_1 L\left(\frac{\bar{r}_s}{z_s}\right) Q\left(\frac{1}{z_s}\right) \exp[-i2\pi\Lambda^{-1}\sqrt{x^2+y^2}]$ respectively. The intensity distributions recorded for a point for a lens (I_{PSF-L}) and an axicon (I_{PSF-A}) are given as

$$I_{PSF-L}(\bar{r}_0;\bar{r}_s,z_s) = \left|\sqrt{I_s/2}C_1 L\left(\frac{\bar{r}_s}{z_s}\right) Q\left(\frac{1}{z_s}\right) \exp\left[- i\pi(\lambda f)^{-1}(x^2+y^2)\right] \otimes Q\left(\frac{1}{z_h}\right)\right|^2, \tag{10}$$

$$I_{PSF-A}(\bar{r}_0;\bar{r}_s,z_s) = \left|\sqrt{I_s/2}C_1 L\left(\frac{\bar{r}_s}{z_s}\right) Q\left(\frac{1}{z_s}\right) \exp\left[- i2\pi\Lambda^{-1}\sqrt{x^2+y^2}\right] \otimes Q\left(\frac{1}{z_h}\right)\right|^2. \tag{11}$$

The point spread function of the system is given as

$$I_{PSF}(\bar{r}_0;\bar{r}_s,z_s) = T_1 \times I_{PSF-L}(\bar{r}_0;\bar{r}_s,z_s) + T_2 \times I_{PSF-A}(\bar{r}_0;\bar{r}_s,z_s), \tag{12}$$

where $0 \le T_1 \le 1$ and $0 \le T_2 \le 1$ control the contributions of lens and axicon respectively. The object intensity distribution can be given by Eq. (7) which is simply $I_{O-L} = I_{PSF-L} \otimes o$ and $I_{O-A} = I_{PSF-A} \otimes o$ for lens and axicon respectively. It is possible to reconstruct o by correlating I_{O-A} and I_{PSF-A} or by correlating I_{O-L} and I_{PSF-L} as shown in Eq. (8). The advantage in the proposed method is that the ARP can be tuned after completing the recording process by tuning T_1 and T_2. It is possible to reconstruct o by processing $I_{O-L} \times T_1 + I_{O-A} \times T_2$ and $I_{PSF-L} \times T_1 + I_{PSF-A} \times T_2$, as $(I_{PSF-L} \times T_1 + I_{PSF-A} \times T_2) \otimes o = I_{O-L} \times T_1 + I_{O-A} \times T_2$.

3. Simulation results

Simulation studies were carried out using MATLAB with a matrix size of 500 × 500 pixels, pixel size $\Delta = 8$ μm, wavelength $\lambda = 632.8$ nm, and $z_h = 30$ cm. Two test objects namely the logos of 'CIPHR' and 'University of Tartu' are considered for the simulation studies. From now on, the two test objects namely the logos of CIPHR and University of Tartu will be addressed as O1 and O2 respectively. Two object planes corresponding to $z_s = 30$ cm and 27 cm were considered. A Diffractive Fresnel Zone Plate (DFZP) with a focal length that do not satisfy the imaging condition was designed such that $\frac{1}{f} \neq \frac{1}{z_s} + \frac{1}{z_h}$. A diffractive axicon with a period of 96 μm was designed to generate a Bessel beam. The images of the test objects O1 and O2 are shown in Figs. 4(a) and 4(b) respectively. The test object O1 and O2 are located in plane 1 ($z_s = 30$ cm) and plane 2 ($z_s = 27$ cm) respectively. Five cases are considered for simulation: ($T_1 = 1$, $T_2 = 0$), ($T_1 = 0.75$, $T_2 = 0.25$), ($T_1 = 0.5$, $T_2 = 0.5$), ($T_1 = 0.25$, $T_2 = 0.75$) and ($T_1 = 0$, $T_2 = 1$) in a fashion of shifting from the characteristics of a lens towards an axicon. The first and fifth cases are pure cases of lens and axicon respectively. The cases in between lens and axicon constitute hybrid imaging system. Let us first consider INCHIS-H1. The amplitude and phase of the diffractive elements for the five cases are shown in Fig. 5. As it is seen in Fig. 5, the hybrid cases have both magnitude as well as phase matrices. The axial distributions were calculated for the five cases by processing the $I_{PSF}(z_s = 30$ cm) with $I_{PSF}(20\ cm \le z_s \le 30\ cm)$ with a step size of 1 mm using NLR with $\alpha = 0$ and $\beta = 1$. In the calculation of axial characteristics, NLR has been used as it is stable and does not require calibration for different cases of intensity distributions like LR^{2}A.

The axial profiles for the five cases are plotted in Fig. 6(a1). As it can be seen, there is a non-linear change in ARP when the values of T_1 and T_2 were varied. The axial distribution for the case ($T_1 = 0$, $T_2 = 1$) resembled the typical axial intensity distribution of an axicon [42,43]. The axial distribution for the case ($T_1 = 1$, $T_2 = 0$) resembled that of a lens. In between these two cases, mixed axial properties formed by combination of different degrees of lens and axicon are obtained. The area under the axial curve is inversely related to the ARP. The normalized areas under the axial curves for different combinations of T_1 and T_2 are plotted as a bar chart in Fig. 6(a2). The plot of the normalized area under the axial curve quantitively shows the difference in ARP for different combinations of T_1 and T_2 with a maximum ARP for a lens ($T_1 = 1$, $T_2 = 0$) and minimum ARP for an axicon ($T_1 = 0$, $T_2 = 1$). The image of the $I_{PSF}(z_s = 30$ cm), $I_{PSF}(z_s = 27$ cm), I_O and their reconstructions at the two planes $I_R(z_s = 30$ cm) and $I_R(z_s = 27$ cm) using LR^{2}A for ($T_1 = 1$, $T_2 = 0$), ($T_1 = 0.75$, $T_2 = 0.25$), ($T_1 = 0.5$, $T_2 = 0.5$), ($T_1 = 0.25$, $T_2 = 0.75$) and ($T_1 = 0$, $T_2 = 1$) are shown in Figs. 6(b)–6(f), Figs. 6(g)–6(k), Figs. 6(l)–6(p), Figs. 6(q)–6(u) and Figs. 6(v)–6(z) respectively.

Comparing the reconstruction results for the different cases, it is seen

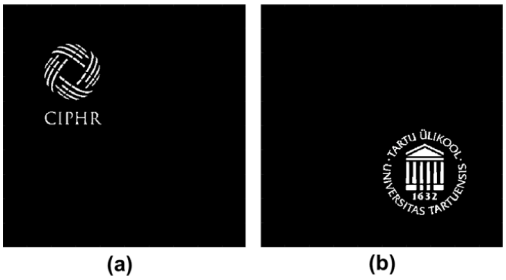

Fig. 4. (a) CIPHR logo and (b) logo of University of Tartu used as test objects O1 and O2 located at $z_s = 30$ cm and $z_s = 27$ cm respectively.

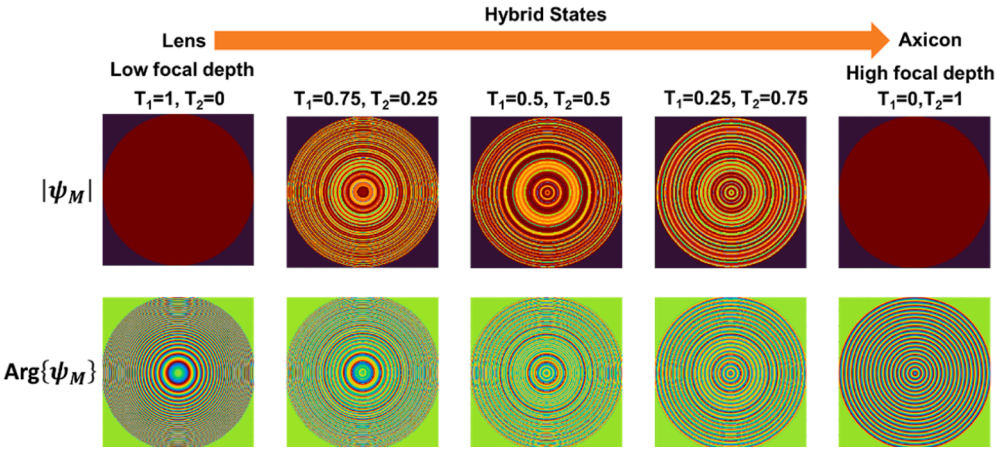

Fig. 5. Magnitude and phase of the diffractive element for ($T_1 = 1$, $T_2 = 0$), ($T_1 = 0.75$, $T_2 = 0.25$), ($T_1 = 0.5$, $T_2 = 0.5$), ($T_1 = 0.25$, $T_2 = 0.75$) and ($T_1 = 0$, $T_2 = 1$) for INCHIS-H1.

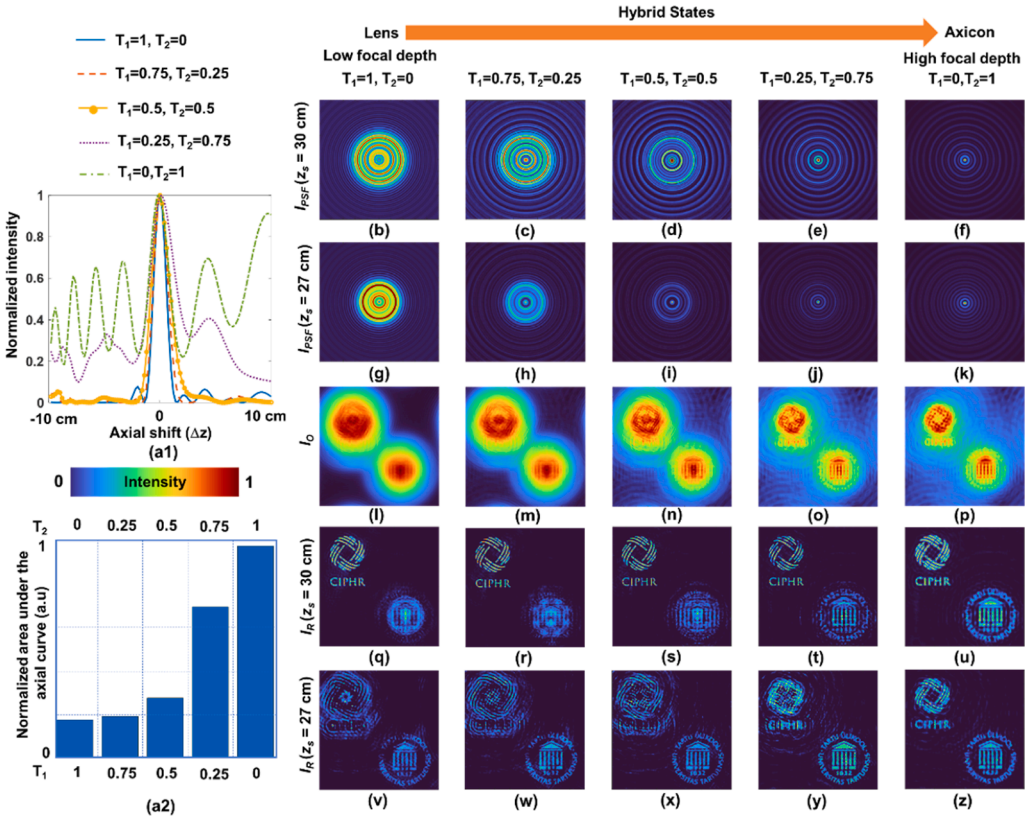

Fig. 6. INCHIS-H1: (a1) Axial intensity distributions for ($T_1 = 1$, $T_2 = 0$), ($T_1 = 0.75$, $T_2 = 0.25$), ($T_1 = 0.5$, $T_2 = 0.5$), ($T_1 = 0.25$, $T_2 = 0.75$) and ($T_1 = 0$, $T_2 = 1$). (a2) Plot of normalized area under the curve for different values of T_1 and T_2. The simulated images of the $I_{PSF}(z_s = 30$ cm), $I_{PSF}(z_s = 27$ cm), I_O and their reconstructions at the two planes $I_R(z_s = 30$ cm) and $I_R(z_s = 27$ cm) using LR^{2}A are shown in 6(b)–6(z). The depth of focus is gradually increased and ARP is gradually decreased as the element is changed from lens to axicon through hybrid states.

that as the values of T_1 and T_2 were tuned to transform the lens into an axicon through hybrid states, the ARP decreased. Comparing Figs. 6(q)–6(u), it is seen the O2 is defocused in the case of 6(q) but the focus improved as the system is shifted towards Fig. 6(u). The same can be observed in Figs. 6(v)–6(z) where the object O1 appear defocused at 6 (v) and it gradually improved as the system is shifted towards 6(z). The above effect can also be achieved by increasing the number of beams with different axial characteristics instead of tuning the strength of the two interfering beams. The optimal values of reconstruction using LR^{2}A for the above cases were $\alpha = 0$, $0.5 \leq \beta \leq 0.6$ and $4 \leq p \leq 10$. Simulation of two points located axially away by 6 cm and moving in circular path with different radii with one clockwise and another counter clockwise was carried out for three cases ($T_1 = 1$, $T_2 = 0$), ($T_1 = 0.5$, $T_2 = 0.5$), and ($T_1 = 0$, $T_2 = 1$). The videos of the I_O and I_R for the above three cases are given in media files S1, S2, S3, S4, S5 and S6 respectively.

INCHIS-H2 as discussed in Section 2, is a post-processing method where two images or two videos, one with a lens and another with an axicon are recorded and combined after applying different weights to the two images or videos using variables T_1 and T_2. When a PSF with a similar combination from lens and axicon is used to reconstruct images and videos, a desirable AR can be obtained. The axial distributions were calculated for the five cases by processing the $I_{PSF}(z_s = 30$ cm) with $I_{PSF}(20\ cm \leq z_s \leq 30\ cm)$ with a step size of 1 mm using NLR with $\alpha = 0$ and $\beta = 1$. The plot of the axial curve for ($T_1 = 1$, $T_2 = 0$), ($T_1 = 0.75$, $T_2 = 0.25$), ($T_1 = 0.5$, $T_2 = 0.5$), ($T_1 = 0.25$, $T_2 = 0.75$) and ($T_1 = 0$, $T_2 = 1$) are shown in Fig. 7(a1). It can be seen from Fig. 7(a1), the gradual increase of focal depth with increase in T_2 and decrease in T_1 as expected. The normalized areas under the axial curves for different

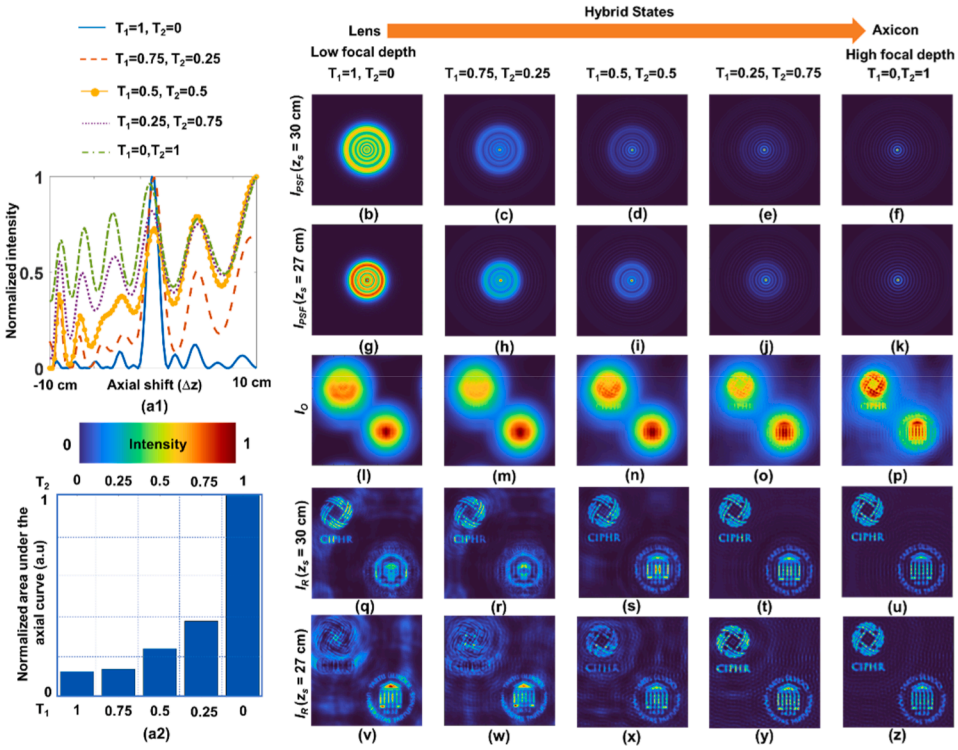

Fig. 7. INCHIS-H2: (a1) Axial intensity distributions for ($T_1 = 1$, $T_2 = 0$), ($T_1 = 0.75$, $T_2 = 0.25$), ($T_1 = 0.5$, $T_2 = 0.5$), ($T_1 = 0.25$, $T_2 = 0.75$) and ($T_1 = 0$, $T_2 = 1$). (a2) Plot of normalized area under the curve for different values of T_1 and T_2. The simulated images of the I_{PSF} ($z_s = 30$ cm), I_{PSF} ($z_s = 27$ cm), I_O and their reconstructions at the two planes I_R ($z_s = 30$ cm) and I_R ($z_s = 27$ cm) using LR^{2}A are shown in 7 (b)–7(z). The depth of focus is gradually increased and ARP is gradually decreased as the element is changed from lens to axicon through hybrid states.

combinations of T_1 and T_2 are plotted as a bar chart in Fig. 7(a2). The plot of the normalized area under the axial curve quantitively shows the difference in ARP for different combinations of T_1 and T_2 with a maximum for a lens ($T_1 = 1$, $T_2 = 0$) and minimum for an axicon ($T_1 = 0$, $T_2 = 1$).

The image of the $I_{PSF}(z_s = 30$ cm), $I_{PSF}(z_s = 27$ cm), I_O and their reconstructions at the two planes $I_R(z_s = 30$ cm) and $I_R(z_s = 27$ cm) using LR^{2}A for ($T_1 = 1$, $T_2 = 0$), ($T_1 = 0.75$, $T_2 = 0.25$), ($T_1 = 0.5$, $T_2 = 0.5$), ($T_1 = 0.25$, $T_2 = 0.75$) and ($T_1 = 0$, $T_2 = 1$) are shown in Figs. 7(b)–7(f), Figs. 7(g)–7(k), Figs. 7(l)–7(p), Figs. 7(q)–7(u) and Figs. 7(v)–7(z) respectively. Comparing the Figs. 7(b)–7(f), Figs. 7(g)–7(k) and Figs. 7(l)–7(p) the transition from the lens to an axicon is evident. Comparing Figs. 7(q)–7(u) and Figs. 7(v)–7(z), the object in the plane of PSF is reconstructed, while the object in the other plane is not reconstructed well. However, as the system is tuned towards axicon, both objects are reconstructed. The optimal values of reconstruction using LR^{2}A for the above cases were $\alpha = 0$, $0.6 \leq \beta \leq 0.7$ and $4 \leq p \leq 10$. Simulation of two points located axially away by 3 cm and moving in circular path with different radii with one clockwise and another counter clockwise was carried out for ($T_1 = 0.5$, $T_2 = 0.5$). The videos of the I_O and I_R for ($T_1 = 0.5$, $T_2 = 0.5$) are given in media files S7 and S8 respectively.

4. Experiments

A photograph of the experimental setup is shown in Fig. 8. The set up was built with a high-power LED (Thorlabs, 940 mW, $\lambda = 660$ nm and $\Delta\lambda = 20$ nm), spatial light modulator (SLM) (Thorlabs Exulus HD2, 1920 × 1200 pixels, pixel size = 8 μm) and an image sensor (Zelux CS165MU/M 1.6 MP monochrome CMOS camera, 1440 × 1080 pixels with pixel size ~3.5 μm), refractive lens ($f = 50$ mm), United States Air Force (USAF) object or pinhole, beam splitter, iris and polarizer. The object is critically illuminated using a refractive lens L1. The I_{PSF} was recorded using a pinhole of diameter 50 μm. The objects USAF objects '1′ and '3′ from Group 5 were used. The light from the object was collimated using a refractive lens L2, and polarized along the active axis of the SLM using a polarizer and passed through the beam splitter to be incident on

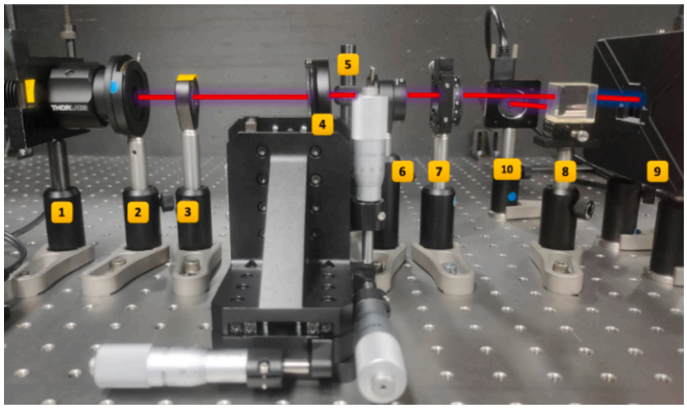

Fig. 8. Photograph of the experimental setup: (1) LED, (2) iris, (3) refractive lens L1 ($f = 50$ mm), (4) object/pinhole, (5) iris, (6) refractive lens L2 ($f = 50$ mm), (7) polarizer (8) beam splitter, (9) SLM, (10) image sensor. (The red line shows the path of the beam from LED to image sensor).

the SLM normally. The phase masks designed for five combinations ($T_1 = 0$, $T_2 = 1$), ($T_1 = 0.25$, $T_2 = 0.75$), ($T_1 = 0.5$, $T_2 = 0.5$), ($T_1 = 0.75$, $T_2 = 0.25$), and ($T_1 = 1$, $T_2 = 0$) moving from axicon to lens are shown in Figs. 9(a1)−9(a5) respectively. On the SLM, phase masks were displayed one after another and the object intensity distributions are recorded by the image sensor. The phase masks were engineered with a DoF < 10%. The MATLAB codes for applying TAP-GSA is provided in supplementary code 1.

The images of the I_{PSF}s for $z_s = 5$ cm and 5. 6 cm for the five cases are shown in Figs. 9(b1)-9(b5) and Figs. 9(c1)-9(c5) respectively. To demonstrate 3D imaging, the I_O of object '3' recorded at ($z_s = 5$ cm) for all the five cases were summed with the corresponding I_O of object '1' recorded at ($z_s = 5.6$ cm) as shown in Figs. 9(d1) to 9(d5). The reconstruction results I_R ($z_s = 5$ cm) shown in Figs. 9(e1) to 9(e5) and I_R ($z_s = 5.6$ cm) shown in Figs. 9(f1) to 9(f5) respectively. The direct image of the object is shown in Fig. 9(g). In 3D imaging, it can be seen that the reconstructed plane appears focused while the other plane is not and the blur increases from axicon towards lens. To quantitatively show the variation of ARP for different values of T_1 and T_2, the normalized ratio between the average intensity values at the two planes given as $S = \frac{\mu_{I_R}(O_1)}{\mu_{I_R}(O_2)}$, where O_1 is the object that is out of focus and O_2 is the object that is in focus during reconstruction, is plotted as shown in Fig. 10. Additional experiments with synthetic objects generated by shifting a point object has been carried out and the results of blurring and 3D experiments are shown in the first section of the supplementary document. This study was carried out using binary phase masks. The MATLAB codes for LR^{2}A are provided in supplementary code 2.

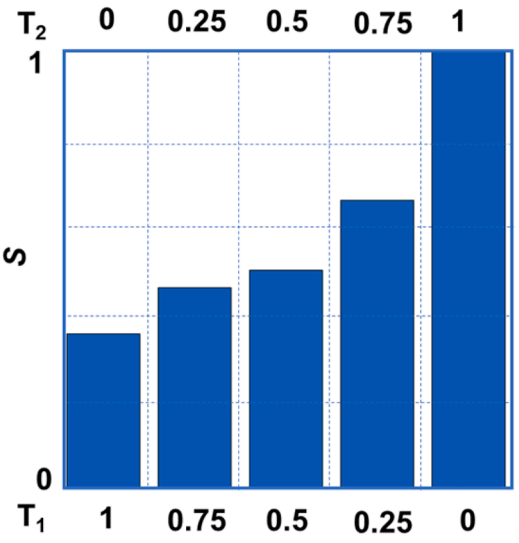

Fig. 10. INCHIS-H1: Normalized ratio S for ($T_1 = 1$, $T_2 = 0$), ($T_1 = 0.75$, $T_2 = 0.25$), ($T_1 = 0.5$, $T_2 = 0.5$), ($T_1 = 0.25$, $T_2 = 0.75$), and ($T_1 = 0$, $T_2 = 1$).

For INCHIS-H2, the recorded images of axicon and lens are combined

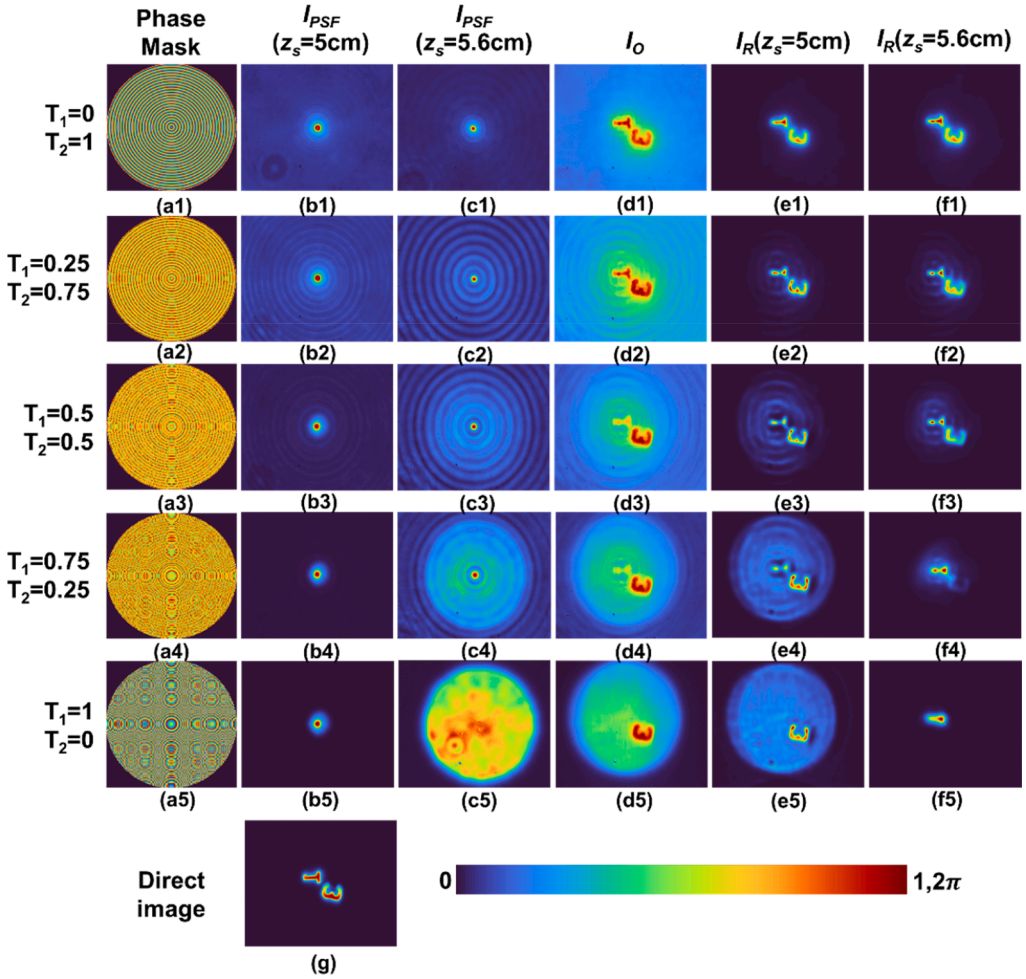

Fig. 9. INCHIS-H1: Phase masks, $I_{PSF}(z_s = 5$ cm), $I_{PSF}(z_s = 5.6$ cm), I_O, reconstruction results $I_R(z_s = 5$ cm) and $I_R(z_s = 5.6$ cm) for: ($T_1 = 0$, $T_2 = 1$), ($T_1 = 0.25$, $T_2 = 0.75$), ($T_1 = 0.5$, $T_2 = 0.5$), ($T_1 = 0.75$, $T_2 = 0.25$), and ($T_1 = 1$, $T_2 = 0$) are shown from Figures (a1) to (a5), (b1) to (b5), (c1) to (c5), (d1) to (d5), (e1) to (e5), and (f1) to (f5), respectively. (g) Direct image when both objects are in the same plane.

after applying different weights to the two images using T_1 and T_2. In the first step, the I_{PSF} of a particular plane ($z_s = 5$ cm) of lens and axicon were taken and the weights $T_1 = 0.25$ and $T_2 = 0.75$ were applied and summed to obtain the I_{PSF} for the second case ($T_1 = 0.25$, $T_2 = 0.75$). Similarly, the I_O of axicon and lens were taken and the weights $T_1 = 0.25$ and $T_2 = 0.75$ were applied and summed to obtain the I_O for the second case ($T_1 = 0.25$, $T_2 = 0.75$). This process was repeated by applying different weights to I_{PSF} and I_O for the other cases. The 3D imaging results are shown in Fig. 11. The images of the I_{PSF}s for $z_s = 5$ cm and 5.6 cm for the five cases are shown in Figs. 11(a1)-11(a5) and Figs. 11(b1)-11(b5) respectively. A second plane information I_O of object '3' recorded at ($z_s = 5$ cm) for all the five cases was summed with the corresponding I_O of object '1' as shown in Figs. 11(c1) to 11(c5). The reconstruction results I_R ($z_s = 5$ cm) are shown in Figs. 11(d1) to 11(d5) and the reconstruction results I_R ($z_s = 5.6$ cm) are shown in Figs. 11(f1) to 11(f5) respectively for the five cases. It can be seen from the above figures that the plane of interest appears focused while the blur of the other plane increases from axicon to lens. In all the above studies, LR^{2}A was operated with $0.3 \leq \alpha \leq 0.6$, $\beta = 1$ and $25 \leq p \leq 35$. To quantitatively show the variation of ARP for different values of T_1 and T_2, the normalized ratio between the average intensity values at the two planes given as S is plotted as shown in Fig. 12. Additional experiments using synthetic objects have been carried out using binary phase masks and the blurring and 3D experiments are presented in the first section of the supplementary section. A proof-of-concept experiment using only refractive elements namely refractive lens and solid axicon was carried out using multiple point objects. The results are presented in the second section of the supplementary document. Once again, the capability to tune ARP was demonstrated.

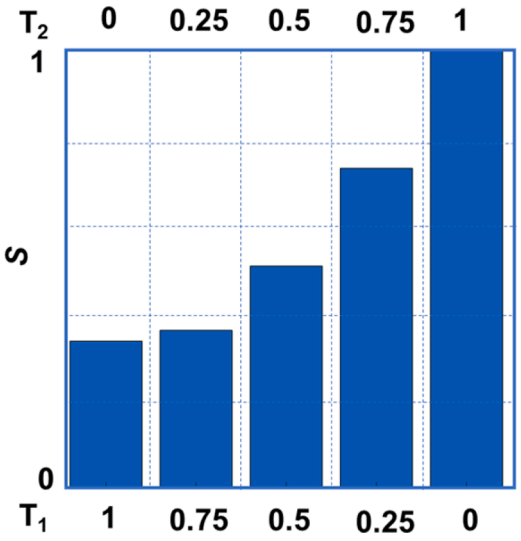

Fig. 12. INCHIS-H2: Normalized ratio S for ($T_1 = 1$, $T_2 = 0$), ($T_1 = 0.75$, $T_2 = 0.25$), ($T_1 = 0.5$, $T_2 = 0.5$), ($T_1 = 0.25$, $T_2 = 0.75$), and ($T_1 = 0$, $T_2 = 1$).

5. Discussion

In this study, two hybridization methods INCHIS-H1 and INCHIS-H2 are proposed and demonstrated. INCHIS-H1 was inspired from [19], but more advanced than [19] with respect to all the characteristics of imaging and the implementation. The method proposed in [19] was based

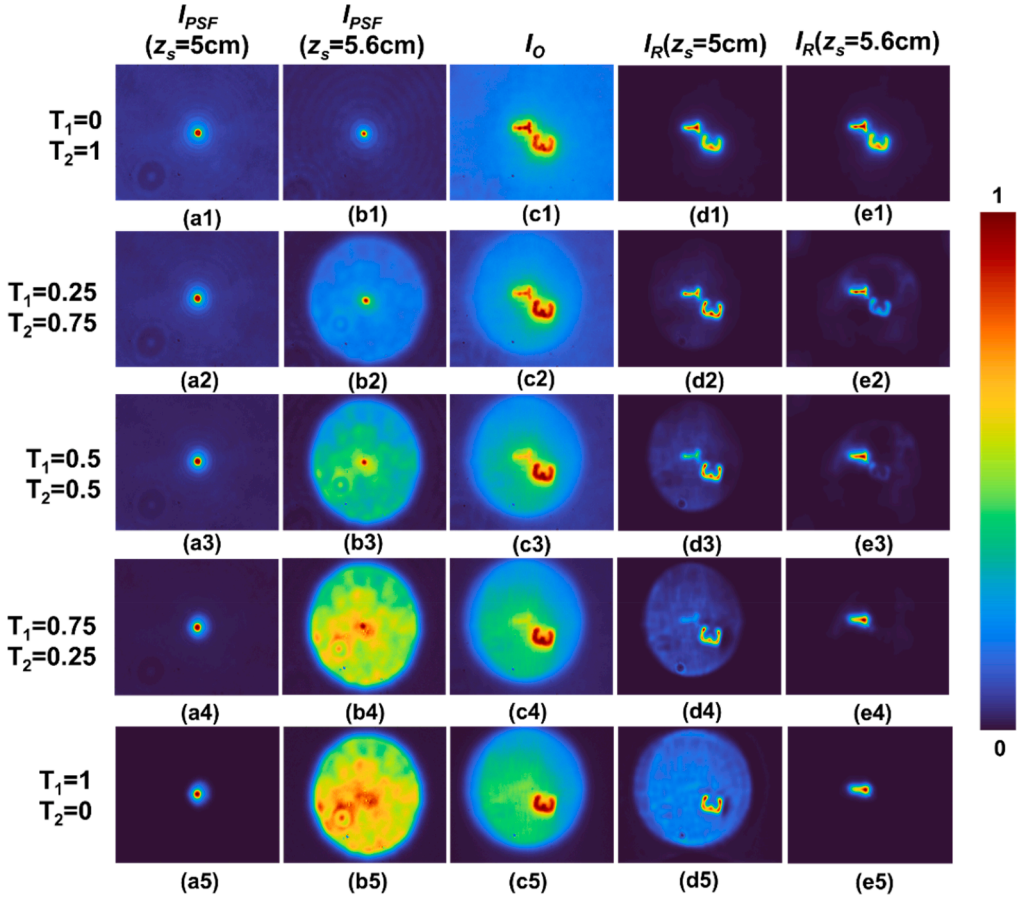

Fig. 11. INCHIS-H2: $I_{PSF}(z_s = 5$ cm), $I_{PSF}(z_s = 5.6$ cm), I_O, reconstruction results $I_R(z_s = 5$ cm) and $I_R(z_s = 5.6$ cm) for: ($T_1 = 0$, $T_2 = 1$), ($T_1 = 0.25$, $T_2 = 0.75$), ($T_1 = 0.5$, $T_2 = 0.5$), ($T_1 = 0.75$, $T_2 = 0.25$), and ($T_1 = 1$, $T_2 = 0$) are shown from Figures (a1) to (a5), (b1) to (b5), (c1) to (c5), (d1) to (d5), (e1) to (e5), and (f1) to (f5), respectively.

on FINCH and COACH and so it was necessary to convert every object point into at least three beams: spherical, plane and chaotic, and at least three camera shots were required. In the proposed INCHIS-H1, every object point is converted into two beams: spherical and Bessel and a single camera shot is sufficient. In a way, the INCHIS method-H1 can be considered FINCH or IDH where the self-interference happens between a Bessel beam and a spherical beam instead of between two spherical beams. By tuning the ratios T_1 and T_2, INCHIS-H1 can be tuned from I-COACH or CAI with lens as coded aperture to I-COACH or CAI with axicon as coded aperture through FINCH. Further, the SNR in the new method is higher than [19]. The above is partially due to the nature of the self-interfering beams, i.e., in the INCHIS-H1, intensity distributions have higher energy density due to deterministic optical fields in comparison to a scattered beam in COACH. The second reason for a better SNR in INCHIS-H1 compared to COACH is the lower photon budget requirement due to lesser number of beams in INCHIS-H1 than COACH. Finally, TAP-GSA is used in INCHIS-H1 for multiplexing phase masks instead of random multiplexing. Finally, in [19], when the ARP is tuned, LRP is also changed unlike in INCHIS methods. In all the hybrid cases, the DoF of TAP-GSA was low to avoid any loss of light due to scattering. The comparison between INCHIS-H1 with FINCH—COACH system, I-COACH with an ensemble of Bessel, Airy and self-rotating beams are provided in section – 3 of the supplementary document.

Ideally, as the phase mask is tuned from a lens ($T_1 = 1$, $T_2 = 0$) to an axicon ($T_1 = 0$, $T_2 = 1$), the focal depth is expected to improve and on average, this is true. However, there are also anomalous axial regions as seen in Fig. 6(a) when the axial response does not follow the expected trend locally. In these regions, the reconstruction of images for a phase mask that contains a higher composition of lens than axicon is of better quality than a phase mask with higher composition of axicon than lens with an I_{PSF} that is recorded for a different plane. Such local axial regions are the anomalous axial regions. In binary phase masks, there is an increase in the occurrence of anomalous axial regions due to higher diffraction orders as seen in the supplementary document. The axial profiles for the five cases ($T_1 = 1$, $T_2 = 0$), ($T_1 = 0.75$, $T_2 = 0.25$), ($T_1 = 0.5$, $T_2 = 0.5$), ($T_1 = 0.25$, $T_2 = 0.75$) and ($T_1 = 0$, $T_2 = 1$) are plotted for a binary phase mask as shown in Fig. 13. As The anomalous axial regions are highlighted with a red dotted circle with yellow glow. In these regions, the variation in AR for different cases do not follow the expected trend. The above problem needs to be addressed in the future studies.

INCHIS-H2 is relatively more elegant and also more powerful compared to INCHIS-H1. The post processing of the recorded intensity distributions involving the addition of the intensity distributions with weights T_1 and T_2, do not create any anomalous axial regions in simulation studies Fig. 7(a1). In simulation studies, the values of T_1 and T_2 in creating the hybrid I_{PSF} and I_O were the same. In experiment, however, it

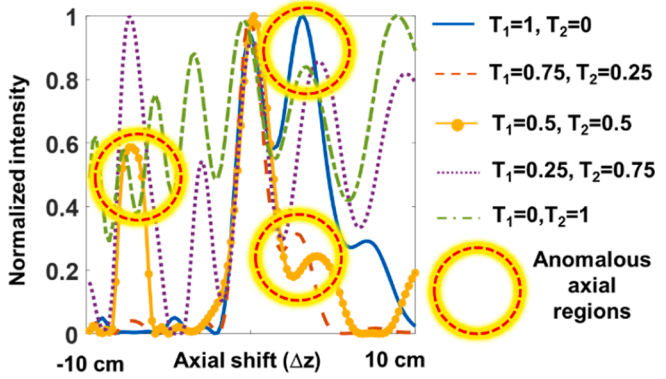

Fig. 13. Axial intensity distributions for ($T_1 = 1$, $T_2 = 0$), ($T_1 = 0.75$, $T_2 = 0.25$), ($T_1 = 0.5$, $T_2 = 0.5$), ($T_1 = 0.25$, $T_2 = 0.75$) and ($T_1 = 0$, $T_2 = 1$) for a binary phase element. The anomalous axial regions are indicated by a red dotted circle with yellow glow.

was necessary to change the values of T_1 and T_2 to compensate the changes made to the exposure time and light intensity during recording. This new method allows to tune the AR of recorded pictures and videos. As with any new method, the advantage often comes with a penalty and INCHIS-H2 is not an exception. The ability to tune the AR of recorded pictures and videos in INCHIS-H2 comes with a penalty which is the need for recording two pictures and two videos instead of one. However, considering the advantages of INCHIS-H2 and considering that most in-line holography methods require at least three camera shots, the penalty is mild.

Conclusion

Two hybridization methods named INCHIS-H1 and INCHIS-H2 have been developed to tune the ARP independent of LRP. In INCHIS-H1, the well-known FINCH configuration has been adapted where the light from an object point is split into two and modulated by a lens and an axicon and self-interfered. A phase mask is designed by multiplexing the functions of a diffractive lens and a diffractive axicon using TAP-GSA to generate a spherical beam and a Bessel beam which are interfered in the image sensor. The contributions of the diffractive lens and diffractive axicon can be tuned using weights such that the system can be tuned between the imaging characteristics of a diffractive lens and that of a diffractive axicon. The simulation and proof-of-concept experimental results are promising. The axial characteristics of the hybrid phase masks varied as predicted theoretically but with some local anomalous regions where the properties crossed over between different cases.

The second method INCHIS-H2 involves recording an object with two elements namely lens and an axicon and they are combined with different weights after recording to obtain a desired ARP. The INCHIS-H2 is more attractive than INCHIS-H1 as it allows to modify the AR of recorded pictures and videos which is significant and is reported for the first time. This new capability to tune ARP will be useful in many applications such as microscopy, computer vision, motion photography and computational imaging. In both methods, INCHIS-H1 and INCHIS-H2, ARP is changed for a constant LRP defined by $\sim\lambda/\mathrm{NA}$. The limit of ARP is set at $\sim\lambda/\mathrm{NA}^2$ which can be reduced to the ARP of axicon but not improved beyond $\sim\lambda/\mathrm{NA}^2$. The LRP can be changed only by conventional means such as changing the NA or changing the size of the pinhole used for recording the I_{PSF}.

Changing LRP of a recorded picture has been reported mostly based on interpolation, extrapolation, deep learning [44–46] and deconvolution methods [34]. Modifying the ARP of recorded videos and pictures had been impossible so far. With the development of the INCHIS-H2, it is possible to modify the ARP of recorded pictures and videos. The study using the SLM has been extended to the configuration shown in Fig. 2 using refractive lens and axicon and the proof-of-concept results are presented in the second section of the supplementary document. But some recent developments on recording virtual I_{PSF} and unusual ring-shaped point spread functions using wavefront modulation gives hope for a better future for INCHIS [47]. Further studies are needed on improving the optical architecture, phase masks and computational reconstruction methods to fully exploit the potential of the developed new hybridization methods. We believe that the developed technology will add new capabilities to imaging.

Funding

This research was funded by the European Union's Horizon 2020 research and innovation program, grant agreement No. 857627 (CIPHR).

CRediT authorship contribution statement

Shivasubramanian Gopinath: Data curation, Investigation, Methodology, Project administration, Software, Validation, Visualization,

Writing – review & editing. **Aravind Simon John Francis Rajeswary:** Data curation, Investigation, Methodology, Project administration, Software, Validation, Visualization, Writing – original draft, Writing – review & editing. **Vijayakumar Anand:** Conceptualization, Data curation, Formal analysis, Funding acquisition, Investigation, Methodology, Project administration, Resources, Software, Supervision, Visualization, Writing – original draft, Writing – review & editing.

Declaration of Competing Interest

The authors declare the following financial interests/personal relationships which may be considered as potential competing interests: Vijayakumar Anand reports financial support was provided by European Union.

Data availability

Data will be made available on request.

Supplementary materials

Supplementary material associated with this article can be found, in the online version, at doi:10.1016/j.optlaseng.2023.107837.

References

[1] Barrett HH, Myers KJ. Foundations of image science. Wiley Series in Pure and Applied Optics (Wiley; 2004.
[2] Khonina SN, Kazanskiy NL, Karpeev SV, Butt MA. Bessel beam: significance and applications–a progressive review. Micromachines (Basel) 2020;11:997.
[3] Zhai Z, He X, Yu X, Liu D, Lv Q, Xiong Z, Wang X, Xu Z. Parallel Bessel beam arrays generated by envelope phase holograms. Opt Laser Eng 2023;161:107348.
[4] Anand V, Rosen J, Juodkazis S. Review of engineering techniques in chaotic coded aperture imagers. Light: Adv Manuf 2022;3:1–13.
[5] Indebetouw G. Nondiffracting optical fields: some remarks on their analysis and synthesis. J Opt Soc Am A 1989;6:150–2.
[6] Dharmavarapu R, Bhattacharya S, Juodkazis S. Diffractive optics for axial intensity shaping of Bessel beams. J Opt 2018;20(8):085606.
[7] Smith D, Ng SH, Han M, Katkus T, Anand V, Glazebrook K, Juodkazis S. Imaging with diffractive axicons rapidly milled on sapphire by femtosecond laser ablation. Appl Phys B 2021;127:154.
[8] Davidson N, Friesem AA, Hasman E. Holographic axilens: high resolution and long focal depth. Opt Lett 1991;16:523–5.
[9] Gorelick S, Paganin DM, De Marco A. Axilenses: refractive micro-optical elements with arbitrary exponential profiles. APL Photonics 2020;5:106110.
[10] Rosen J, Yariv A. Snake beam: a paraxial arbitrary focal line. Opt Lett 1995;20:2042–4.
[11] Latychevskaia T, Fink H-W. Inverted Gabor holography principle for tailoring arbitrary shaped three-dimensional beams. Sci Rep 2016;6:26312.
[12] Rosen J, Vijayakumar A, Kumar M, Rai MR, Kelner R, Kashter Y, Bulbul A, Mukherjee S. Recent advances in self-interference incoherent digital holography. Adv Opt Photon 2019;11:1–66.
[13] Liu JP, Tahara T, Hayasaki Y, Poon TC. Incoherent digital holography: a review. Appl Sci 2018;8:143.
[14] Tahara T, Zhang Y, Rosen J, Vijayakumar A, Cao L, Wu J, Koujin T, Matsuda A, Ishii A, Kozawa Y, Okamoto R, Oi R, Nobukawa T, Choi K, Imbe M, Poon T-C. Roadmap of incoherent digital holography. Appl Phys B 2022;128:193.
[15] Rosen J, Brooker G. Digital spatially incoherent Fresnel holography. Opt Lett 2007;32:912–4.
[16] Brooker G, Siegel N, Wang V, Rosen J. Optimal resolution in Fresnel incoherent correlation holographic fluorescence microscopy. Opt Express 2011;19:5047–62.
[17] Bouchal P, Bouchal Z. Selective edge enhancement in three-dimensional vortex imaging with incoherent light. Opt Lett 2012;37:2949–51.
[18] Vijayakumar A, Kashter Y, Kelner R, Rosen J. Coded aperture correlation holography—A new type of incoherent digital holograms. Opt Express 2016;24:12430–41.
[19] Vijayakumar A, Kashter Y, Kelner R, Rosen J. Coded aperture correlation holography (COACH) system with improved performance [Invited]. Appl Opt 2017;56:F67–77.
[20] Ables JG. Fourier transform photography: a new method for X-ray astronomy. Publ Astron Soc Aust 1968;1:172–3.
[21] Dicke RH. Scatter-hole cameras for X-rays and gamma rays. Astrophys J 1968;153:L101–6.
[22] Fenimore EE, Cannon TM. Coded aperture imaging with uniformly redundant arrays. Appl Opt 1978;17:337–47.
[23] Chi W, George N. Optical imaging with phase-coded aperture. Opt Express 2011;19:4294–300.
[24] Horisaki R, Ogura Y, Aino M, Tanida J. Single-shot phase imaging with a coded aperture. Opt Lett 2014;39:6466–9.
[25] Vijayakumar A, Rosen J. Interferenceless coded aperture correlation holography—A new technique for recording incoherent digital holograms without two-wave interference. Opt Express 2017;25:13883–96.
[26] Horner JL, Gianino PD. Phase-only matched filtering. Appl Opt 1984;23(6):812–6.
[27] Rai MR, Vijayakumar A, Rosen J. Non-linear adaptive three-dimensional imaging with interferenceless coded aperture correlation holography (I-COACH). Opt Express 2018;26:18143–54.
[28] Smith D, et al. Nonlinear reconstruction of images from patterns generated by deterministic or random optical masks—concepts and review of research. J Imaging 2022;8:174.
[29] Anand V, Han M, Maksimovic J, Ng SH, Katkus T, Klein A, Bambery K, Tobin MJ, Vongsvivut J, Juodkazis S. Single-shot mid-infrared incoherent holography using Lucy-Richardson-Rosen algorithm. Opto-Electron Sci 2022;1:210006.
[30] Richardson WH. Bayesian-based iterative method of image restoration. J Opt Soc Am 1972;62:55–9.
[31] Lucy LB. An iterative technique for the rectification of observed distributions. Astron J 1974;79:745–54.
[32] Praveen PA, et al. Deep deconvolution of object information modulated by a refractive lens using Lucy-Richardson-Rosen algorithm. Photonics 2022;9:625.
[33] Gopinath S, et al. Implementation of a large-area diffractive lens using multiple sub-aperture diffractive lenses and computational reconstruction. Photonics 2023;10:3.
[34] Jayavel A, et al. Improved classification of blurred images with deep-learning networks using Lucy-Richardson-Rosen algorithm. Photonics 2023;10:396.
[35] Anand V. Tuning axial resolution independent of lateral resolution in a computational imaging system using Bessel speckles. Micromachines (Basel) 2022;13:1347.
[36] Kumar R, Anand V, Rosen J. 3D single shot lensless incoherent optical imaging using coded phase aperture system with point response of scattered airy beams. Sci Rep 2023;13:2996.
[37] Bleahu A, et al. 3D incoherent imaging using an ensemble of sparse self-rotating beams. Opt Express 2023;31:26120–34.
[38] Rai MR, Rosen J. Depth-of-field engineering in coded aperture imaging. Opt Express 2021;29:1634–48.
[39] Vijayakumar A, Bhattacharya S. Design and fabrication of diffractive optical elements with MATLAB. SPIE; 2017.
[40] Gerchberg RW, Saxton WO. A practical algorithm for the determination of phase from image and diffraction plane pictures. Optik (Stuttg) 1972;35:227–46.
[41] Gopinath S, et al. Enhanced design of multiplexed coded masks for Fresnel incoherent correlation holography. Sci Rep 2023;13:7390.
[42] Brzobohatý O, Čižmár T, Zemánek P. High quality quasi-Bessel beam generated by round-tip axicon. Opt Express 2008;16:12688–700.
[43] Zapata-Rodríguez CJ, Sánchez-Losa A. Three-dimensional field distribution in the focal region of low-Fresnel-number axicons. J Opt Soc Am A 2006;23:3016–26.
[44] Zou Y, Zhang L, Liu C, Wang B, Hu Y, Chen Q. Super-resolution reconstruction of infrared images based on a convolutional neural network with skip connections. Opt Laser Eng 2021;146:106717.
[45] Huang Z, Cao L. Bicubic interpolation and extrapolation iteration method for high resolution digital holographic reconstruction. Opt Laser Eng 2020;130:106090.
[46] Wang B, Zou Y, Zhang L, Li Y, Chen Q, Zuo C. Multimodal super-resolution reconstruction of infrared and visible images via deep learning. Opt Lasers Eng 2022;156:107078.
[47] Yu X, Wang K, Xiao J, Li X, Sun Y, Chen H. Recording point spread functions by wavefront modulation for interferenceless coded aperture correlation holography. Opt Lett 2022;47:409–12.